Simulation of Flow Phenomena at a Rotor with a Discontinuous Galerkin CFD Solver

Fabian Genuit, Manuel Keßler, and Ewald Krämer

Abstract The Discontinuous Galerkin method is a high-order method in space reducing the amount of cells needed for calculations compared to standard computational fluid dynamics (CFD) solvers. At the Institue for Aerodynamics and Gas Dynamics the CFD code SUNWinT has been developed using a DG method with the aim to apply it to rotor flows. The present study concerns the progress in simulating the flow phenomena of an isolated rotor in hover. The results of the calculations are compared to experimental data and show good agreement. Furthermore, the first phenomenological results of the flow around an isolated rotor in forward flight are presented, which reveal promising results and should serve as a starting point for future investigations.

1 Introduction

Nowadays, computational fluid dynamics (CFD) has become a fundamental tool for the analysis of various kinds of flow problems in nature and for technical applications. The demand for precise results and short simulation times is growing as the available computer power has become an easily accessible and still steadily increasing resource. Therefore, High-Performance Computing (HPC) has become a standard tool in CFD. The simulations are performed on several computer processors (CPUs), which on the one hand shortens the time for the calculation. On the other hand, the parallelization of the simulation requires a communication between the CPUs which may become a bottleneck in terms of computation duration. Classical CFD methods like the finite volume (FV) method need to work on smooth and highly resolved meshes in order to produce reliable results. The creation of these computational meshes is usually a time-consuming process. Furthermore, the spatial order of accuracy of the FV method stagnates at second order due to an inefficiently high parallel communication effort in highly parallel calculations.

F. Genuit (✉) · M. Keßler · E. Krämer
Institute of Aerodynamics and Gas Dynamics, University of Stuttgart, Pfaffenwaldring 21, 70569 Stuttgart, Germany
e-mail: genuit@iag.uni-stuttgart.de

W. E. Nagel et al. (eds.), *High Performance Computing in Science and Engineering '19*,
https://doi.org/10.1007/978-3-030-66792-4_26

The Discontinuous Galerkin (DG) method, first used by Reed and Hill [14], has the potential to replace or at least augment the classical CFD methods. The advantage of DG is that the mesh resolution is less restrictive than for FV solvers because the spatial accuracy order may be chosen arbitrarily. Additionally, the parallelization of the DG method requires less communication effort. In fluid mechanics the DG method combines the ideas of the finite element (FE) and the FV methods. The approach of the method is based on the FE Galerkin discretization scheme in which the solution within a cell is given by a polynomial approximation of arbitrary order. In contrast to a classical FE discretization, the DG approach allows the solution to be discontinuous between the cells. Hence, a solver for that kind of Riemann problem is required, which is well known from FV methods.

The DG solver SUNWinT (Stuttgart University Numerical Wind Tunnel) has been developed at the Institute for Aerodynamics and Gas Dynamics (IAG) in the past 15 years. Landmann [9] introduced the first basic functionalities (up to the discretization of the RANS equations) in 1D and 2D space. In [10] Lübon implemented 3D functionality and a method for Detached Eddy Simulations (DES). Afterwards, Wurst [18] improved the solver and extended it for moving bodies in 2D space. This work will consistently pursue the global objective of the project: the turbulent simulation of a helicopter rotor considering of fluid-structure interaction.

Yang and Yang [20] presented results of the Euler flow around an isolated rotor using a DG solver with an overset grid method and third order. In this work first 3D simulations of a moving, isolated rotor in hover with the IAG DG solver SUNWinT have been performed. The results of fourth order are compared with the experimental data provided by Caradonna and Tung [4]. Furthermore, a first approach of the DG simulation of the flow around an isolated rotor in forward flight is presented.

2 Governing Equations

To determine the physics of a fluid in motion, conservation of mass, momentum and energy are required. If viscous, compressible flows the so-called Navier–Stokes equations are considered

$$\frac{\partial \mathbf{U}}{\partial t} + \nabla \left(\mathbf{F}_{inv}(\mathbf{U}) - \mathbf{F}_{vis}(\mathbf{U}, \nabla \mathbf{U}) \right) = \mathbf{S}(\mathbf{U}, \nabla \mathbf{U}) \tag{1}$$

describe their physical behavior. In Eq. (1) the state vector of conservative variables $\mathbf{U}$, the inviscid flux tensor $\mathbf{F}_{inv} = (\mathbf{F}^x_{inv}\ \mathbf{F}^y_{inv}\ \mathbf{F}^z_{inv})^T$ and the viscous flux tensor $\mathbf{F}_{vis} = (\mathbf{F}^x_{vis}\ \mathbf{F}^y_{vis}\ \mathbf{F}^z_{vis})^T$ read as

$$\mathbf{U} = \begin{pmatrix} \rho \\ \rho u_i \\ \rho E \end{pmatrix}, \quad \mathbf{F}^j_{\text{inv}}(\mathbf{U}) = \begin{pmatrix} \rho u_j \\ \rho u_i u_j + p\delta_{ij} \\ (\rho E + p)\, u_j \end{pmatrix}, \quad \mathbf{F}^j_{\text{vis}}(\mathbf{U}, \nabla\mathbf{U}) = \begin{pmatrix} 0 \\ \tau_{ij} \\ u_i \tau_{ji} + q_j \end{pmatrix}. \tag{2}$$

ρ represents the density, u_i the components of the velocity vector, p the pressure and E the specific total energy. To achieve a well-defined solution of the conservative variables, another equation is necessary describing the state of the fluid. The present work deals with air as the working fluid, which is assumed to be a perfect gas with a constant specific heat ratio $\kappa = 1.4$. Thus, the equation of state for ideal gases is used and can be written as a connection between the pressure p and the specific total energy E

$$p = (\kappa - 1)\left(\rho E - \frac{1}{2}\rho \sum_{i=1}^{N_{\text{DIM}}} u_i^2\right). \tag{3}$$

Since air is considered a Newtonian fluid, the Stokes hypothesis is valid and the viscous stress tensor τ in (2) becomes symmetrical $\tau_{ij} = \tau_{ji}$. The entries are described as a function of the velocity gradients and the dynamic viscosity μ

$$\tau_{ij} = \mu\left(\frac{\partial u_i}{\partial x_j} + \frac{\partial u_j}{\partial x_i} - \frac{2}{3}\frac{\partial u_k}{\partial x_k}\delta_{ij}\right). \tag{4}$$

The energy flux vector $\mathbf{q}$ can be determined by Fourier's law

$$q_j = -\lambda \frac{\partial T}{\partial x_j} \tag{5}$$

where the thermal conductivity coefficient λ is assumed to be isotropic. λ can be expressed as a function of temperature, dynamic viscosity and the non-dimensional Prandtl number Pr

$$\lambda = \frac{\mu c_p}{Pr} \qquad \text{with } Pr = 0.72 \quad (\text{for air with } 200K \leq T \leq 700K). \tag{6}$$

In Eq. (1), the source term $\mathbf{S}$ exists only for some specific applications, as it will be introduced in Sect. 4.

In [19], Wurst has already shown that the governing equations can easily be extended to the RANS equations with appropriate closure models for turbulence modeling beyond the scope of this work, which only considers inviscid and laminar flows.

3 Numerical Formulation

3.1 Spatial Discretization

The DG method is used to discretize the governing Eq. (1) in space. Since the DG method is a combination of the FV and the FE method, the starting point is a classical FE approach. The unknown conservative variables $\mathbf{U}$ are approximated on the basis of piecewise polynomial ansatz functions

$$\mathbf{U}(\mathbf{x}, t) \approx \widetilde{\mathbf{U}}(\mathbf{x}, t) = \sum_{i=1}^{N_b} \mathbf{u}_i(t)\phi_i(\mathbf{x}) \tag{7}$$

with N_b basis functions $\phi_i(\mathbf{x})$ of a polynomial order p only depending on space [7]. In contrast, the unknown degrees of freedom $\mathbf{u}_i(t)$ are time-dependent.

Next, Eq. (7) is substituted into the Navier–Stokes equation (1) and multiplied by an arbitrary test function

$$\mathbf{v}(\mathbf{x}) = \mathbf{v}_h(\mathbf{x}) = \sum_{j=1}^{N_b} \mathbf{a}_j \phi_j(\mathbf{x}). \tag{8}$$

In the case of the FE Galerkin approach, the basis functions for the approximate solution $\widetilde{\mathbf{U}}$ and the test function are selected equally ($\phi_i = \phi_j$). The values a_j in equation are arbitrary. An integration over the whole domain Ω follows, which is approximated with a finite number of elements E. Finally, the integration by parts yields the so-called semi-discrete weak form of the governing equations on the element level

$$\begin{aligned}
&\int_E \mathbf{v}_h \frac{\partial \widetilde{\mathbf{U}}_h}{\partial t} \, \mathrm{d}\Omega \\
&+ \oint_{\partial E} \mathbf{v}_h \left(\mathbf{F}_{\mathrm{inv}}(\widetilde{\mathbf{U}}_h) - \mathbf{F}_{\mathrm{vis}}(\widetilde{\mathbf{U}}_h, \nabla\widetilde{\mathbf{U}}_h) \right) \cdot \mathbf{n} \, \mathrm{d}\sigma \\
&- \int_E \nabla\mathbf{v}_h \cdot \left(\mathbf{F}_{\mathrm{inv}}(\widetilde{\mathbf{U}}_h) - \mathbf{F}_{\mathrm{vis}}(\widetilde{\mathbf{U}}_h, \nabla\widetilde{\mathbf{U}}_h) \right) \, \mathrm{d}\Omega \\
&= \int_E \mathbf{v}_h \, \mathbf{S}(\widetilde{\mathbf{U}}_h, \nabla\widetilde{\mathbf{U}}_h) \, \mathrm{d}\Omega .
\end{aligned} \tag{9}$$

In the equation the index $_h$ marks the discrete functions on the element level. Up to this point there is no difference to a regular FE Galerkin scheme. However, the DG method has no requirements for any kind of continuity properties of the solution

at the element boundaries. Due to the possibility of discontinuities in the solution, the surface integral of the inviscid fluxes is determined with a Harten, Lax and van Leer (HLL) Riemann solver according to [17]. The viscid flux terms have to be treated differently since they are not only dependent on the conservative variables but also on their gradients. For the determination of the gradients the so-called BR2 method, which was developed by Bassi et al. [2], is applied. The integrals in Eq. (9) are approximated numerically by Gaussian integration.

3.2 Temporal Discretization

The spatially discretized Eq. (9) can be written in compact form describe the global equation system

$$\mathbf{M}\frac{\partial \hat{\mathbf{U}}}{\partial t} = \mathbf{R}(\widetilde{\mathbf{U}}_h). \tag{10}$$

$\hat{\mathbf{U}}$ denotes the unknown global solution vector and $\mathbf{M}$ the global mass matrix. On the right hand side the residual $\mathbf{R}(\widetilde{\mathbf{U}}_h)$ is composed of the inviscid and viscous fluxes and source terms from Eq. (9).

The temporal integration of Eq. (10) is done using an implicit scheme. The advantage of these schemes is that their stability in relation to the Courant-Friedrichs-Lewy (CFL) condition is theoretically not restricted. Hence, the number of iterations needed until the calculation converges (e.g. to a steady state) is expected to be less than for explicit schemes. However, the computational effort is higher and the implementation is more complex. By applying a classical backward Euler method to Eq. (10), it can be rewritten as

$$\mathbf{M}\frac{\hat{\mathbf{U}}(t_{n+1}) - \hat{\mathbf{U}}(t_n)}{\Delta t} = \mathbf{R}\left(\widetilde{\mathbf{U}}(t_{n+1})\right). \tag{11}$$

For the solution of the given nonlinear system, the Newton-Raphson method is used, and leading to

$$\left(\frac{\mathbf{M}}{\Delta t} - \frac{\partial \mathbf{R}\left(\widetilde{\mathbf{U}}(t_{k-1})\right)}{\partial \widetilde{\mathbf{U}}}\right)\Delta\hat{\mathbf{U}} = \mathbf{R}\left(\widetilde{\mathbf{U}}(t_{k-1})\right) - \mathbf{M}\frac{\hat{\mathbf{U}}(t_{k-1}) - \hat{\mathbf{U}}(t_n)}{\Delta t}. \tag{12}$$

In order to solve this equation, several Newton iterations for each time step are required. Starting with the solution from the prior time step $\hat{\mathbf{U}}(t_n) = \hat{\mathbf{U}}(t_{k=0})$, the equation is solved for $\Delta\hat{\mathbf{U}}$ until a required accuracy ϵ is achieved. Then the new solution for the next time step can be determined by

$$\widetilde{\mathbf{U}}(t_{n+1}) = \widetilde{\mathbf{U}}(t_n) + \Delta\widetilde{\mathbf{U}}. \tag{13}$$

Accordingly, for every Newton iteration k a linear system has to be constructed and solved. While the composition of the left and right hand side is done analytically, the linear system is solved by a GMRES solver, preconditioned with an ILU(0) method.

The implicit scheme can be applied in the way it is described above to solve unsteady problems. To achieve a faster convergence for $t \to \infty$, it is modified for steady simulations. Since there is no requirement for time precision, only a single Newton iteration per time step is performed in this case. Furthermore, a local or a global adaption of the time step can be chosen.

4 Arbitrary Lagrangian Eulerian Formulation

The kinematic description of motion for continuum mechanical problems is categorized into the Lagrangian and the Eulerian approach. In the Lagrangian specification of the field each individual node follows the material particle associated while moving. In contrast, in the Eulerian framework, which is mainly used in fluid mechanics, the material moves with respect to a fixed grid.

A combination of both descriptions results in the Arbitrary Lagrangian Eulerian (ALE) formulation, where the nodes of a mesh can either move or be fixed. Thus, a more universal description is attained. Additionally, it can handle any arbitrary velocity of the nodes of the computational grid in order to deal with problems e.g., like fluid-structure interaction. The basic principle of the ALE description can be described with a fixed computational domain Ω_{ref}, in which the governing equations are solved. A mapping $\mathbf{J}(x_{\text{ref}}, t)$ transforms the solution into the actual domain Ω, moving and deforming arbitrarily (see Fig. 1).

Hence, the governing equations have to be reformulated in the ALE space. For a detailed derivation the reader is referred to Persson et al. [13], leading to

$$\frac{\partial (j\mathbf{U})}{\partial t} + \nabla \cdot \left(j\mathbf{U}\mathbf{J}^{-1}\mathbf{F} - j\mathbf{U}\mathbf{J}^{-1}\mathbf{u}_g \right) = j\mathbf{S}. \tag{14}$$

Equation (14) serves as the basis for the DG discretization. As the ALE reference space the local reference space of each element is defined, which is also quite common in the literature [11, 12]. $\mathbf{J}$ respectively its determinant $j = |\mathbf{J}|$ are the mapping quantities from the local reference space to the moving, deformed physical space. The difference compared to the classical Eulerian formulation of the DG method is that the mapping quantities $\mathbf{J}$ and j now have to be calculated in every time step. Furthermore, additional fluxes arising from the grid velocity $\mathbf{u}_g$ have to be considered (see Eq. (14)).

Furthermore, the rotation of the mesh and the rotor investigated is considered rigid. Moreover, if the coordinate system is rotated with the same velocity as the mesh, the mapping quantities $\mathbf{J}$ and j stay constant and have to be calculated only once. Since there is no deformation of the mesh, there is no need to account for geometric conservation aspects. However, an additional source term has to be considered,

describing the pseudo forces due to the rotation of the coordinate system

$$\mathbf{S} = \begin{pmatrix} 0 \\ -\omega \times \rho u_i \\ 0 \end{pmatrix} \tag{15}$$

where ω is the angular velocity of the rotating system. Furthermore, the Riemann solver must be adapted as well as the grid velocity needs to be taken into account (for further details, see [18]).

5 Curved Elements

In classical CFD methods such as the FV method, the discretized domain usually is constructed with straight elements. Consequently, the resolution of curved surfaces on flow bodies is not accurate. This downside is countered by using a high number of cells near the body surface in FV calculations.

However, the DG method requires a lower number of cells, as mentioned in Sect. 1. At the same time the approximation of the solution in each cell becomes more accurate due to the high-order approach. Thus, using curved elements for the representation of curved flow bodies becomes a crucial part when high-order methods are applied. Generally, the high-order solution of curved surfaces with straight elements may not converge at all or could even become unphysical [1].

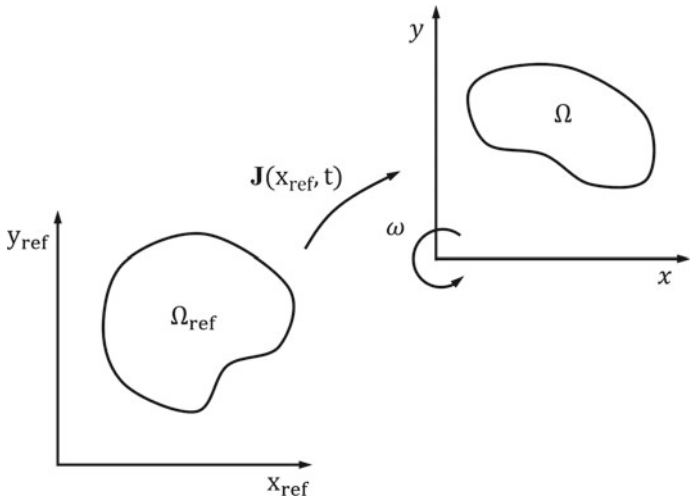

Fig. 1 Mapping between the ALE reference space and the arbitrary moving, physical space [13]

Since standard mesh generators are not able to create curved elements, a plethora of different approaches exists (see [1, 6, 9]) to handle the situation. In this work an agglomeration approach is chosen [6]. Each element of the mesh has a certain number of interpolation points $P^{\mathbf{x}}_{ijk} = (x^{Int}_{ijk}, y^{Int}_{ijk}, z^{Int}_{ijk})$ that contain information about the curvature of the flow body. To transfer this information to the high-order method, a mapping function with a third order Lagrangian polynomial is used. Considering 3D hexahedral elements this leads to 64 interpolation points, which are given as

$$P^{\mathbf{x}_{\text{ref}}}_{ijk} = \left(\frac{1}{3}i, \frac{1}{3}j, \frac{1}{3}k\right) \quad i, j, k \in \{0, 1, 2, 3\} \tag{16}$$

in the reference element. These points are mapped to the interpolations points of the high-order element by

$$\mathbf{x}(x_{\text{ref}}, y_{\text{ref}}, z_{\text{ref}}) = \sum_{i=0}^{3}\sum_{j=0}^{3}\sum_{k=0}^{3} P^{\mathbf{x}}_{ijk} l_i(x_{\text{ref}}) l_j(y_{\text{ref}}) l_k(z_{\text{ref}}) \tag{17}$$

with

$$l_i(x_{\text{ref}}) = \prod_{\substack{0 \le m \le 3 \\ m \neq n}} \frac{x_{\text{ref}} - x_{ref,i}}{x_{ref,i} - x_{ref,m}}. \tag{18}$$

$l_j(y_{\text{ref}})$ and $l_k(z_{\text{ref}})$ are analogous. These mapping quantities are also considered in the Jacobian $\mathbf{J}$ and its determinant j as introduced in Eq. (14).

6 Numerical Setup and Results

Since the validation of the above properties of our code was already provided in [15, 18], progress was made to perform calculations of a more advanced problem. In order to keep the complexity of the flow problem simple for the beginning, the simulation of a rigid rotor blade in hover was performed. By analyzing the results from these calculations, experience is gained with the difficulties of the case and later on the complexity of the problem can be gradually increased.

The numerical setup used for the simulations in this work is based on the experimental study of Caradonna and Tung [4]. The two bladed rotor uses a NACA0012 profile and is untapered and untwisted. In Fig. 2a the geometrical setup of one single blade is shown, where the aspect ratio of the outer blade radius R to the chord length c is $\frac{R}{c} = 6$. In the model the inner blade radius r_i was chosen to be $r_i = c$. In order to simplify the mesh generation of the two bladed rotor, a solid connection between both blades was constructed as it is illustrated in Fig. 2b with a view from the top onto the discretized domain. Obviously, the rotor hub was neglected. The collective pitch angle for each blade was set to $\alpha = 5°$.

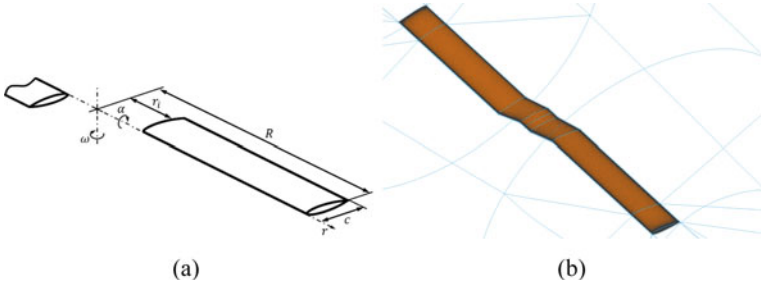

Fig. 2 Geometric (**a**) and numerical setup (**b**) of the rotor of Caradonna and Tung [4]

The numerical setup has about 560,000 hexahedral, curved elements (see Sect. 5). The distance of the outer boundary is twelve times the rotor radius and is chosen to be a farfield condition. For now, a slip wall boundary condition is chosen for the blade surfaces. Additionally, the Reynolds number is set to $Re = 10{,}000$ to expect a laminar flow since no appropriate turbulence model has been implemented yet. Although these conditions are not completely consistent with the experiment from Caradonna and Tung, their results were consulted as a reference.

6.1 Isolated Rotor in Hover

The simulation of the rigid rotor setup in hover was performed with a steady, implicit time integration scheme using the technique presented in Sect. 4 with a rotating coordinate system, which is a valid method as Krämer showed in [8]. The tip Mach number was set to $Ma_{tip} = 0.226$. With these settings simulations in ascending order up to four (p3) were performed.

The Q criterion was employed to visualize vortex structures, which are illustrated for isosurfaces of Q in Fig. 3a. The typical tip vortices convecting with the induced flow of the rotor are visible. Furthermore, the contraction of the rotor wake can clearly be seen. Figure 3b, c show the results for the pressure coefficient c_p over the chord length for different blade sections at $\frac{r}{R} = 0.68$ and $\frac{r}{R} = 0.96$ with the fourth order of accuracy (p3). Even though the blade surface is considered a slip wall, the comparison to the experimental data of [4] shows good agreement especially for the outer blade sections.

6.2 Isolated Rotor in Forward Flight

With respect to the work of Stangl [16], the numerical setup introduced above was used in a further study to perform the simulation of a rotor in forward flight.

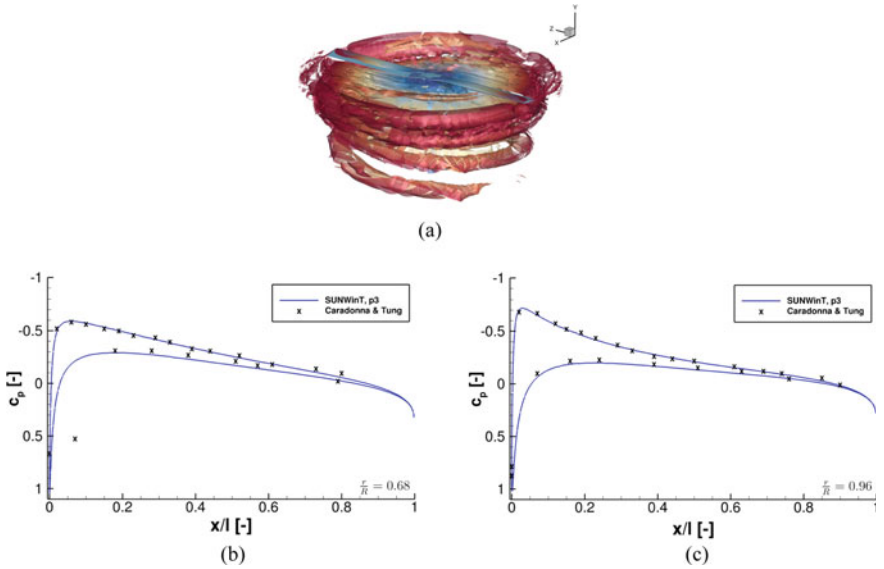

Fig. 3 Isosurfaces for the Q criterion (**a**) and pressure coefficient c_p at a blade section of $\frac{r}{R} = 0.68$ (**b**) and $\frac{r}{R} = 0.96$ (**c**) for the rotor in hover

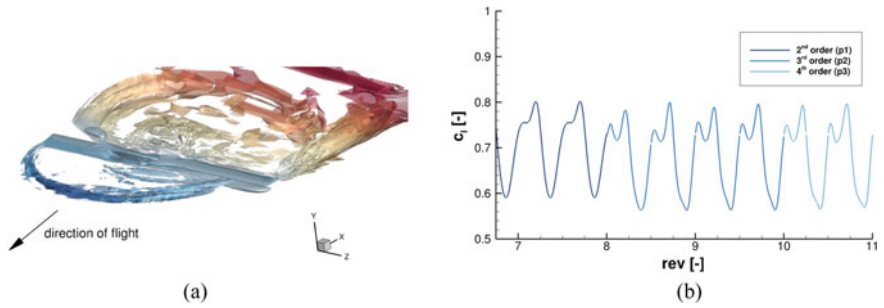

Fig. 4 Isosurfaces for the Q criterion (**a**) and lift coefficient c_l (**b**) for the rotor in forward flight

However, the collective pitch angle of $\alpha = 5°$ was not varied during the rotation of the rotor blade. Accordingly, an untrimmed rotor behavior with high roll moments was expected and observed. The simulations were executed with the unsteady, implicit time integration scheme for spacial orders up to four (p3). The advance ratio was chosen on $\mu = 0.2$, while the tip Mach number had a value of $Ma_{\text{tip}} = 0.25$.

In Fig. 4a, the isosurfaces for the Q criterion again depicts the vortices in the rotor wake. The blade-vortex interaction is visible, which is typical for a rotor in forward flight. This interaction is also observed in Fig. 4b, where the lift coefficient is plotted over the rotor revolution. Obviously, the interaction of the blade vortex with

the following blade occurs twice each complete rotor revolution. With increasing accuracy order, the impact of the interaction on the lift coefficient is better resolved.

The purpose of these simulations was to verify the functionality of the solver with this kind of flow problem, which succeeded. Furthermore, the typical phenomenological effects of a rotor in forward flight were demonstrated.

7 Computational Performance

The promising parallel performance of the solver was reported previously for various cases with explicit calculations in [3] and even with implicit calculations in [19]. Hence, the simulation of rotating rigid bodies should essentially behave similarly as there is no additional effort in communication compared to a classical simulation without the ALE formulation and the curved element approach. As a test case a cycling sphere with radius $r = 0.5\,\mathrm{m}$ was chosen, using 14,400 curved hexahedral elements.

Figure 5a shows the strong scaling of the case with $\omega = 0.01\,^1/_\mathrm{s}$, which causes a flow velocity of $Ma = 0.2$ at the sphere for simulations with an accuracy of second to forth order. Since the number of degrees of freedoms (DOFs) increases with the

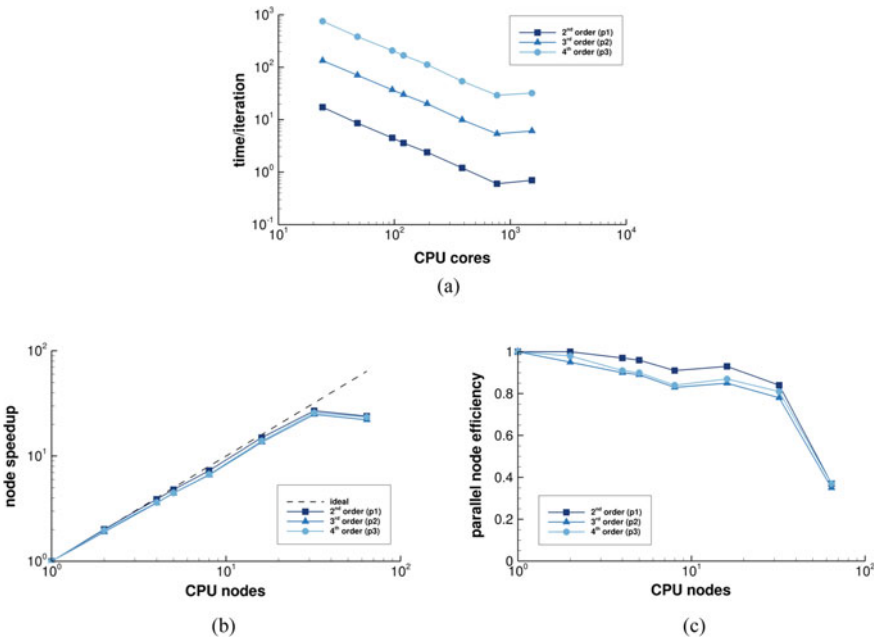

Fig. 5 Strong scaling (**a**), node speedup (**b**) and parallel node efficiency (**c**) for different orders of accuracy

accuracy order, it is obvious that the time per iteration increases. However, SUNWinT scales almost linearly for all orders. The calculation at 1536 cores indicates the limit of an efficient parallel execution. At this point the communication effort exceeds the local workload and thus the computational time increases.

Due to the memory required for the composition of the global system matrix, in this case a single core calculation was only possible with second order. Hence, a pseudo-speedup with computational nodes (1 node consists of 24 cores) was applied. In Fig. 5b the node speedup shows almost ideal behaviour for all accuracy orders that were investigated. The drop of the speedup for 64 nodes once again indicates the limit of the parallel work distribution. The parallel node efficiency in Fig. 5c reveals a slightly better performance for the second order calculations, whereas the behavior for third and fourth order is almost identical. Generally, the parallel efficiency stays above a value of 80% for a wide node range.

Finally, the focus is on the dependence of these performance results of the linear system solver. As introduced in Sect. 3.2, a GMRES solver with an ILU(0) preconditioner is employed, which is provided by the trilinos package [5] preinstalled at the CRAY XC40 system at HLRS. Thus, the performance of this iterative solver strongly influences the performance of the code and is identified as a crucial component.

8 Conclusion

The Navier–Stokes equations have been discretized with a DG method and extended with an ALE formulation to allow moving and deforming domains. Furthermore, the importance of an accurate representation of the flow body surface on a high-order method was discussed. The experiment of Caradonna and Tung [4] served as a test case for the first series of simulations of an isolated rotor in hover. Even though a few assumptions were made, it was shown that SUNWinT works in principle for these types of flow problems. The results were in good agreement with the experimental data and the typical flow phenomena at a rotor in hover have been detected. Moreover, the simulation of an isolated rotor with a constant pitch angle in forward flight confirms the phenomenologically expected results.

However, the aim of current and future work is to extend the code to fully turbulent simulations of multi-bladed rotors. Furthermore, the Chimera method will be employed, as it was introduced in [19] for 2D problems.

References

1. F. Bassi, S. Rebay, High-order accurate discontinuous finite element solution of the 2D Euler equations. J. Comput. Phys. **138**, 251–285 (1997)
2. F. Bassi, A. Crivellini, S. Rebay, M. Savini, Discontinuous Galerkin solution of the Reynolds-averaged-Navier–Stokes and k-w turbulence model equations. Comput. Fluids **34** (2005)

3. E.R. Busch, M. Wurst, M. Keßler, E. Krämer, Computational aeroacoustics with higher order methods, in *High Performance Computing in Science and Engineering '12*, ed. by W.E. Nagel, D.H. Kröner, M.M. Resch (Springer, Berlin, 2013)
4. F. Caradonna, C. Tung, Experimental and analytical studies of a model helicopter rotor in hover. Technical report TM 81232, NASA (1981)
5. M.A. Heroux, R.A. Bartlett, V.E. Howle, R.J. Hoekstra, J.J. Hu, T.G. Kolda, R.B. Lehoucq, K.R. Long, R.P. Pawlowski, E.T. Phipps et al., An overview of the Trilinos project. ACM Trans. Math. Softw. (TOMS) **31**(3), 397–423 (2005)
6. F. Hindenlang, Mesh curving techniques for high order parallel simulations on unstructured meshes. Ph.D. thesis, Institut für Aerodynamik und Gasdynamik, Universität Stuttgart (2014)
7. G.E. Karniadakis, S.J. Sherwin (eds.), *Spectral/hp Element Methods in CFD* (Oxford University Press, Oxford, 1999)
8. E. Krämer, Theoretische Untersuchungen der stationären Rotorblattumströmung mit Hilfe eines Euler–Verfahrens. Dissertation, Institut für Luftfahrttechnik und Leichtbau, Universität der Bundeswehr München (1991)
9. B. Landmann, A parallel discontinuous Galerkin code for the Navier–Stokes and Reynolds-averaged Navier–Stokes equations. Ph.D. thesis, Insitut für Aerodynamik und Gasdynamik, Universität Stuttgart (2008)
10. C. Lübon, Turbulenzmodellierung und Detached Eddy Simulation mit einem Discontinuous Galerkin Verfahren von hoher Ordnung. Ph.D. thesis, Institut für Aerodynamik und Gasdynamik, Universität Stuttgart (2009)
11. D.J. Mavriplis, C.R. Nastase, On the geometric conservation law for high-order discontinuous Galerkin discretizations on dynamically deforming meshes. J. Comput. Phys. **230**(11), 4285–4300 (2011). Special issue High Order Methods for CFD Problems
12. C.A.A. Minoli, D.A. Kopriva, Discontinuous Galerkin spectral element approximations on moving meshes. J. Comput. Phys. **230**(5), 1876–1902 (2011)
13. P.-O. Persson, J. Bonet, J. Peraire, Discontinuous Galerkin solution of the Navier–Stokes equations on deformable domains. Comput. Methods Appl. Mech. Eng. **198**(17–20), 1585–1595 (2009)
14. W.H. Reed, T.R. Hill, Triangular mesh methods for the neutron transport equation. Technical report, Los Alamos Scientific Laboratory (1973)
15. L. Schmitt, Erweiterung eines Discontinuous-Galerkin-Verfahrens auf rotierende Gitter (2012)
16. R. Stangl, Ein Euler–Verfahren zur Berechnung der Strömung um einen Hubschrauber im Vorwärtsflug. Dissertation, Institut für Aerodynamik und Gasdynamik, Universität Stuttgart (1996)
17. E.F. Toro, *Riemann Solvers and Numerical Methods for Fluid Dynamics: A Practical Introduction*, 2nd edn. (Springer, Berlin, 1999)
18. M. Wurst, Development of a high-order Discontinuous Galerkin CFD solver for moving bodies. Ph.D. thesis, Institut für Aerodynamik und Gasdynamik, Universität Stuttgart (2016)
19. M. Wurst, M. Kessler, E. Krämer, *A High-Order Discontinuous Galerkin Chimera Method for the Euler and Navier–Stokes Equations* (Chap. II.2) (2015), pp. 423–433
20. L. Yang, A. Yang, Implementation of spectral difference method on overset grids for compressible inviscid flows. Comput. Fluids **140**, 500–511 (2016)